

The impact of anisotropy from finite light travel time on detecting ionized bubbles in redshifted 21-cm maps.

Suman Majumdar^{1*}, Somnath Bharadwaj^{1†}, Kanan K. Datta^{2‡} and T. Roy Choudhury^{3§}

¹*Department of Physics and Meteorology & Centre for Theoretical Studies, IIT, Kharagpur 721302, India*

²*The Oskar Klein Centre for Cosmoparticle Physics & Department of Astronomy, Stockholm University, Albanova, SE-10691 Stockholm, Sweden*

³*Harish-Chandra Research Institute, Chhatnag Road, Jhusi, Allahabad 211019, India*

25 October 2021

ABSTRACT

The detection of ionized bubbles around quasars in redshifted 21-cm maps is possibly one of the most direct future probes of reionization. We consider two models for the growth of spherical ionized bubbles to study the apparent shapes of the bubbles in redshifted 21-cm maps, taking into account the finite light travel time (FLTT) across the bubble. In both models the bubble has a period of rapid growth beyond which its radius either saturates or grows slowly. We find that the FLTT, whose effect is particularly pronounced for large bubbles, causes the bubble’s image to continue to grow well after its actual growth is over. There are two distinct FLTT distortions in the bubble’s image: (i) its apparent center is shifted along the line of sight (LOS) towards the observer from the quasar; (ii) it is anisotropic along the LOS. The bubble initially appears elongated along the LOS. This is reversed in the later stages of growth where the bubble appears compressed.

The FLTT distortions are expected to have an impact on matched filter bubble detection where it is most convenient to use a spherical template for the filter. We find that the best matched spherical filter gives a reasonably good estimate of the size and the shift in the center of the anisotropic image. The mismatch between the spherical filter and the anisotropic image causes a degradation in the SNR relative to that of a spherical bubble. The degradation is in the range 10 – 20% during the period of rapid growth when the image appears elongated, and is less than 10% in the later stages when the image appears compressed.

We conclude that a spherical filter is adequate for bubble detection. The FLTT distortions do not affect the lower limits for bubble detection with 1000 hr of GMRT observations. The smallest spherical filter for which a detection is possible has comoving radii 24 Mpc and 33 Mpc for a 3σ and 5σ detection respectively, assuming a neutral fraction 0.6 at $z \sim 8$.

Key words: methods: data analysis - cosmology: theory: - diffuse radiation

1 INTRODUCTION

According to our current understanding, reionization of neutral hydrogen (H I) is most likely an extended process operating over redshifts $6 \lesssim z \lesssim 15$ and is most likely driven by stellar sources forming within galaxies (for reviews, see Choudhury & Ferrara 2006; Choudhury 2009). The H I distribution at these epochs is characterized by ionized bubbles centered around galaxies, with characteristic sizes determined by the efficiency of photon production and the clustering properties of the galaxies (Furlanetto, Zaldarriaga & Hernquist, 2004). These bubbles overlap as reionization proceeds, and the H II (ionized hydrogen) distribution develops a complex

topology. Statistical probes of the redshifted 21-cm signal, like the power spectrum (see Furlanetto, Oh & Briggs 2006 for a review) and the bispectrum (Bharadwaj & Pandey, 2005), carry signatures of these bubbles. A detection of the statistical signal would indirectly constrain the bubble distribution. In contrast, it would be possible to directly probe this by detecting the individual H II regions.

At this moment it is not clear whether the first generation of 21-cm observations would be able to detect the detailed topology of H II regions and constrain reionization histories. Most likely, the present day instruments (GMRT¹ (Swarup et al., 1991)) or those expected in the near future (e.g., MWA², LOFAR³) might just be adequate for detecting the presence or absence of an ionized region. The first target could possibly be detection of H II bubbles

* E-mail: sumanm@phy.iitkgp.ernet.in

† E-mail: somnath@phy.iitkgp.ernet.in

‡ E-mail: kdatt@astro.su.se

§ E-mail: tirth@hri.res.in

¹ <http://www.gmrt.ncra.tifr.res.in>

² <http://www.haystack.mit.edu/ast/arrays/mwa/>

³ <http://www.lofar.org/>

around targeted luminous sources (say, quasars) which can have much larger sizes than the typical galaxy generated ionized regions. The growth of such a region may, in the simplest situation, be modeled as a spherical ionized bubble embedded in a uniform neutral medium and its growth can be followed analytically (Shapiro & Giroux, 1987). The redshifted H I 21-cm signal from such a bubble will be buried in foregrounds and noise, both of which are considerably larger than the signal. Further the noise in different pixels of a radio interferometric image is correlated. It is a big challenge to detect this faint redshifted 21-cm signal of an ionized bubble. Datta, Bharadwaj & Choudhury (2007) (hitherto Paper I) have developed a visibility based matched filter technique that optimally combines the H I signal of an extended bubble while removing foregrounds and minimizing the noise. The analysis shows that density fluctuations in the neutral hydrogen outside the bubble impose a limit on the comoving radius of the smallest bubble that can be detected. This limit is independent of the observing time. Simulations show (Datta, Majumdar, Bharadwaj & Choudhury 2008; hitherto Paper II) that bubbles of comoving radius ≤ 6 Mpc and ≤ 12 Mpc cannot respectively be detected using the GMRT and the MWA respectively, however large be the observing time. In addition, it is also possible to show that the redshift $z \sim 8$ is optimum for bubble detection (Datta, Bharadwaj & Choudhury 2009; hitherto Paper III). At the redshift $z = 8$, for a bubble located at the center of the field of view (FoV), it will be possible to detect (3σ) a bubble of comoving radius ≥ 19 Mpc and ≥ 22 Mpc with 1000 hrs of observation using the GMRT and MWA respectively provided the gas outside the bubble is completely neutral. This prediction is somewhat modified if a significant fraction of the neutral gas outside the bubble is ionized by $z \sim 8$. In a situation where the neutral hydrogen fraction outside the bubble is $x_{H\text{I}} \sim 0.6$ at $z = 8$ (Choudhury & Ferrara, 2006; Choudhury, 2009), the comoving radius of the smallest bubble that can be detected in 1000 hrs of observation is ~ 24 Mpc and ~ 28 Mpc for the GMRT and MWA respectively.

Most of the analysis of matched filter bubble detection (Papers I, II and III) assumes the ionized region to be a spherical bubble. However, a growing spherical bubble will appear anisotropic for a present day observer due to the finite light travel time (FLTT) (Wyithe & Loeb, 2004; Yu, 2005; Wyithe, Loeb & Barnes, 2005; Shapiro et al., 2006; Sethi & Haiman, 2008), and due to the evolution of the global ionized fraction (Geil et al., 2008). These anisotropies, if detected, would provide important information about the quasar luminosity and the evolution of the global ionization fraction. While this is an interesting possibility, it is unlikely that it will be feasible to discern such details using either the present day instruments (GMRT) or those expected in the near future. (eg. MWA) which are just adequate for detecting the presence or absence of an ionized bubble. Given this, it would be most appropriate to search for ionized regions using a spherical bubble as a template in the matched filter technique. The search can either be completely blind where we vary the four parameters $[\theta_x, \theta_y, z_b, R_b]$, or it can be targeted along a known quasar where it is sufficient to vary $[z_b, R_b]$. Here θ_x, θ_y, z_b are respectively the two angular coordinates and redshift of the bubble center, while R_b is the bubble's comoving radius. In the matched filter analysis, the signal to noise ratio is maximum when the parameters of the filter exactly match those of the bubble actually present in the data. In other words, a detection is achieved by varying the parameters of the filter so that it is exactly matched to the signal of the bubble that is actually present in the data. The apparent anisotropies will, however, introduce a mismatch between the signal and the filters. This is potentially a serious issue for both a blind search and targeted bubble detection.

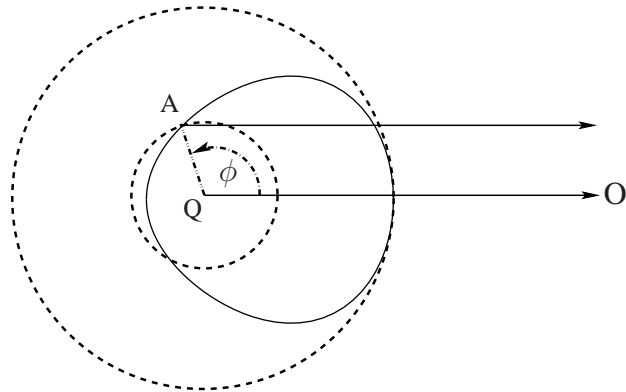


Figure 1. The dashed lines show different stages of the growing H II bubble around a quasar Q. The solid curve shows the apparent shape of the H II bubble for a distant observer O located in the direction indicated by the arrows.

In this paper we study the impact of this apparent anisotropy on our ability to detect ionized bubbles in a targeted search around a known quasar using the matched filter technique.

In reality apart from these anisotropies the ionized regions around quasars would not be spherical because of various other effects like inhomogeneities in the IGM, overlapping ionized bubbles arising from stellar sources and possible anisotropic emission from the quasar itself. Moreover, the foreground subtraction could also subtract a part of the signal, which may change the recovered bubble shape. The anisotropy in bubble shape caused by these effects would vary from bubble to bubble, and it is rather difficult to incorporate these effects in our analytical estimations, so we do not attempt this here. Geil & Wyithe (2008) and Geil et al. (2008) have studied several of these effects using semi-numerical simulations.

A brief outline of the paper follows. In Section 2. we discuss the equations governing the growth of a spherical ionized bubble and the apparent anisotropy due to the FLTT. Section 3. reviews the matched filter technique for bubble detection. In Section 4. we quantify the apparent anisotropy due to the FLTT and assess its impact on bubble detection. We also discuss the effect of an evolving global neutral fraction. We summarize and conclude in section 5. Growth equation for ionized bubble with an evolving neutral fraction has been discussed in Appendix A.

Unless mentioned otherwise, throughout the paper we present results for the redshift $z = 8$ assuming the neutral hydrogen fraction $x_{H\text{I}} = 0.6$ outside the bubble, with the cosmological parameters $h = 0.74$, $\Omega_m = 0.3$, $\Omega_\Lambda = 0.7$, $\Omega_b h^2 = 0.0223$.

2 GROWTH OF IONIZED BUBBLES AND THEIR APPARENT SHAPE

We first review the equation governing the growth of a spherical H II region around a quasar (Shapiro & Giroux, 1987; White, Becker, Fan & Strauss, 2003; Wyithe & Loeb, 2004; Wyithe, Loeb & Barnes, 2005; Yu, 2005; Shapiro et al., 2006; Sethi & Haiman, 2008). For our purpose we consider the form given in eq. (7) of Yu 2005, which is

$$\frac{4\pi}{3} \frac{d}{d\tau} (x_{H\text{I}} \langle n_H \rangle r^3) = \dot{N}_{\text{phs}}(\tau) - \frac{4}{3} \pi \alpha_B C \langle n_H \rangle^2 r^3. \quad (1)$$

Here the quasar is assumed to be triggered at a cosmic time t_i , and $\tau = t - t_i$ denotes the quasar's age at any later time t . The variable $r(\tau)$ denotes the radius of the spherical ionizing front

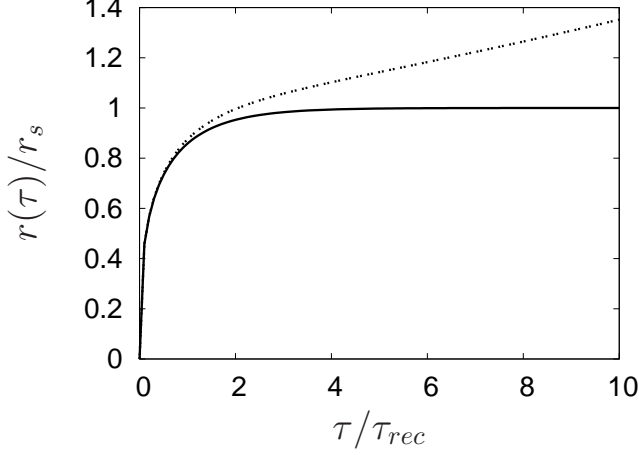


Figure 2. The growth of an H II bubble for Models (i) and (ii) shown by the solid and dashed curves respectively.

(Figure 1) at the instant when a photon that was emitted from the quasar at τ catches up with the ionizing front. The quasar is assumed to emit ionizing photons isotropically at a rate $\dot{N}_{phs}(\tau)$ which completely ionizes the hydrogen inside the spherical bubble of radius $r(\tau)$. The bubble is surrounded by gas with mean hydrogen number density $\langle n_H \rangle$ and neutral fraction $x_{H\ I}$. The term $\alpha_B (= 2.6 \times 10^{-13} \text{ cm}^3 \text{ s}^{-1})$ is the recombination coefficient to excited levels of hydrogen at $T = 10^4 \text{ K}$, and $C \equiv \langle n_{H\ I}^2 \rangle / \langle n_H \rangle^2$ is the clumping factor, which quantifies the effective clumpiness of the hydrogen inside the bubble. Eq. (1) essentially tells us that the growth of the bubble is driven by the supply of ionizing photons after accounting for the photons required to compensate for the recombinations inside the existing ionized region. The effect of Hubble expansion is not included in this equation.

Assuming that all the quantities except $r(\tau)$ and $\dot{N}_{phs}(\tau)$ are constant over the time-scale of the bubble's growth, we have the solution

$$r(\tau) = \left[\frac{3}{4\pi \langle n_H \rangle x_{H\ I}} \int_0^\tau \dot{N}_{phs}(\hat{\tau}) \exp\left(\frac{\hat{\tau} - \tau}{\tau_{rec}}\right) d\hat{\tau} \right]^{\frac{1}{3}} \quad (2)$$

where τ_{rec} is the recombination time defined as

$$\begin{aligned} \tau_{rec} &= x_{H\ I} (C \langle n_H \rangle \alpha_B)^{-1} \\ &\simeq 4 \times 10^6 \text{ yr} \left(\frac{x_{H\ I}}{0.1} \right) \left(\frac{30}{C} \right) \left(\frac{7.4}{1+z} \right)^3. \end{aligned} \quad (3)$$

For the redshift of our interest ($z = 8$) and assuming that $x_{H\ I} = 0.6$ and $C = 30$ (Yu & Lu, 2005) we have $\tau_{rec} \simeq 1.33 \times 10^7 \text{ yr}$ which we use throughout.

Following Yu 2005, we consider two different models for the photon emission rate $\dot{N}_{phs}(\tau)$. In Model (i) $\dot{N}_{phs}(\tau) = \dot{N}_{phs,i}$ is a constant whereas it increases exponentially in Model (ii) $\dot{N}_{phs}(\tau) = \dot{N}_{phs,i} \exp(\tau/\tau_S)$. Here $\tau_S \simeq 4.5 \times 10^7 \text{ yr} \left[\frac{\epsilon}{0.1(1-\epsilon)} \right]$ where τ_S is the Salpeter time-Scale and ϵ is the mass to energy conversion efficiency whose value typically is $\epsilon \simeq 0.1$ which we adopt throughout (Yu & Tremaine, 2002; Yu & Lu, 2004, 2005). This gives $\tau_S \simeq 5 \times 10^7 \text{ yr}$ which we have used throughout in Model (ii). The bubble growth $r(\tau)$ for model (i) and (ii) are respectively given by

$$r(\tau) = r_s \left[1 - \exp\left(-\frac{\tau}{\tau_{rec}}\right) \right]^{\frac{1}{3}} \quad (4)$$

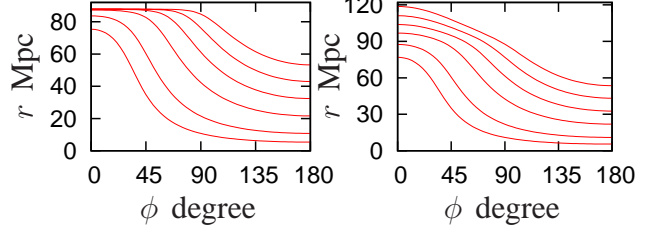


Figure 3. The variation of r with ϕ for Models (i) (left) and (ii) (right) with $r_s = 88 \text{ Mpc}$. In both panels τ_Q takes values $(1.3, 2.7, 5.3, 8.0, 10.6, 13.3) \times 10^7 \text{ yr}$ from the bottom to top. The values of r_s and r are both in comoving Mpc.

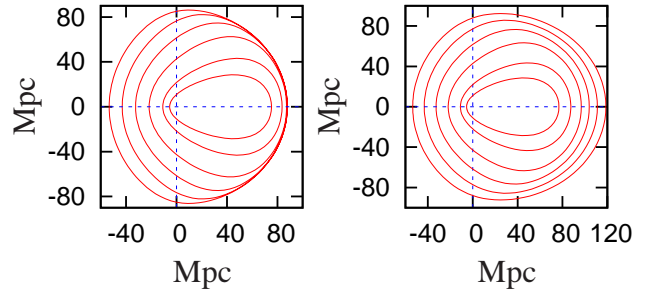


Figure 4. The shape of the H II bubble as it would appear in a redshifted 21-cm map. The distant observer is located to the right of the figure, and the line of sight is along the x axis. The quasar is located at the intersection of the two dashed lines. The photon emission model, r_s and τ_Q values are the same as in Figure 3. The left and right panels correspond to Model (i) and (ii) respectively.

and

$$r(\tau) = r_s \left\{ \left(\frac{\tau_s}{\tau_s + \tau_{rec}} \right) \left[\exp\left(\frac{\tau}{\tau_s}\right) - \exp\left(-\frac{\tau}{\tau_{rec}}\right) \right] \right\}^{\frac{1}{3}} \quad (5)$$

where

$$r_s = \left(\frac{3\dot{N}_{phs,i}\tau_{rec}}{4\pi x_{H\ I} \langle n_H \rangle} \right)^{\frac{1}{3}} \quad (6)$$

for which the solutions are shown in Figure 2. In both models the bubble has an initial period ($\tau < \tau_{rec}$) of rapid growth $r(\tau) \simeq (\tau/\tau_{rec})^{1/3}$. In Model (i) the bubble radius subsequently approaches a constant value $r(\tau) = r_s$. In Model (ii) the bubble radius does not reach a steady value but continues to grow at a slower rate beyond $r > r_s$.

To visualize the apparent shape of the bubble as seen by a present day observer we need the relation between r and ϕ , where ϕ is the angle between observer's line of sight (LOS) and the point A under consideration on the ionization front (Figure 1). The light travel time starting from the quasar at τ to the point A and then to the present day observer is $[r(\tau)/c](1 - \cos \phi)$ more compared to the photon that was emitted from the quasar at age τ_Q and travels straight to the present day observer. This gives

$$\tau_Q = \tau + \frac{r(\tau)}{c} (1 - \cos \phi). \quad (7)$$

(eq. (3) of Yu 2005) which we use along with eq. (4) or eq. (5) to determine r as a function of ϕ for Models (i) and (ii) respectively.

The photons from the front part of the bubble ($\phi < 90^\circ$) take less time to reach the observer as compared to photons from the rear part ($\phi > 90^\circ$). As a consequence the observer sees different parts

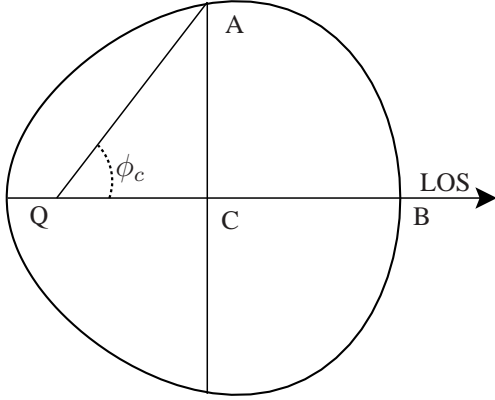


Figure 5. This shows the apparent shape of an H II bubble as it would to a distant observer located along the line of sight (LOS) indicated in the figure. The apparent center of the bubble shifts by $\overline{QC} = \Delta r/2$ from the quasar Q to the point C. The apparent radius is $\overline{CB} = R_{\parallel}$ along the LOS and $\overline{CA} = R_{\perp}$ in the perpendicular direction.

of the bubble at different stages of its growth whereby it appears anisotropic along the LOS.

The apparent shape of the H II region is controlled by the parameters r_s and τ_Q , where τ_Q is the quasar's age as seen by a present day observer. In Figure 3 we have explicitly shown r as a function of ϕ for $r_s = 8 \times c\tau_{rec}(1+z) = 88$ Mpc (comoving) and $\tau_Q/\tau_{rec} = 1, 2, 4, 6, 8, 10$, which correspond to $\tau_Q = (1.3, 2.7, 5.3, 8.0, 10.6, 13.3) \times 10^7$ yr respectively. In Figure 4 we show a radial section through the center of the bubble as it would appear in a redshifted 21-cm map. The difference in light travel time across the bubble is more for larger bubbles, which is why we have chosen a particularly large value of r_s to illustrate the anisotropy. Note that here and in all subsequent discussion we use comoving length-scales.

The bubble grows rapidly when $\tau_Q/\tau_{rec} \leq 1$ which is close to the instant when the quasar was triggered. We then have a large difference between the front and back surfaces (Figure 3). The back surface, is viewed at an earlier phase of growth compared to the front surface. This has mainly two effects on the bubble's apparent shape (Figure 4), (i) the center is shifted along the LOS towards the observer, (ii) the bubble appears anisotropic. We also note that the bubble appears elongated along the LOS in the early stage of growth. The difference between the front and back surfaces gradually comes down with increasing τ_Q . The apparent center then approaches the quasar position, and the elongation along the LOS also diminishes. While Models (i) and (ii) are nearly indistinguishable at small τ_Q , the behavior are somewhat different at large τ_Q .

For a fixed r_s and τ_Q , we use r_{min} and r_{max} to denote the bubble's comoving radius r at $\phi = 180^\circ$ and 0° respectively. The difference $\Delta r = r_{max} - r_{min}$ causes the bubble's center to shift by a comoving distance $\Delta r/2$ relative to the quasar along the LOS towards the observer (Figure 5). The bubble has comoving radii $R_{\parallel} = (r_{max} + r_{min})/2$ and R_{\perp} along the LOS and perpendicular to it respectively (Figure 5). In the subsequent discussion we use R_{\perp} to characterize the comoving size of the anisotropic bubble. The dimensionless ratio

$$s = \frac{\Delta r}{2R_{\perp}} \quad (8)$$

expresses the shift in the bubble's center as a fraction of its radius

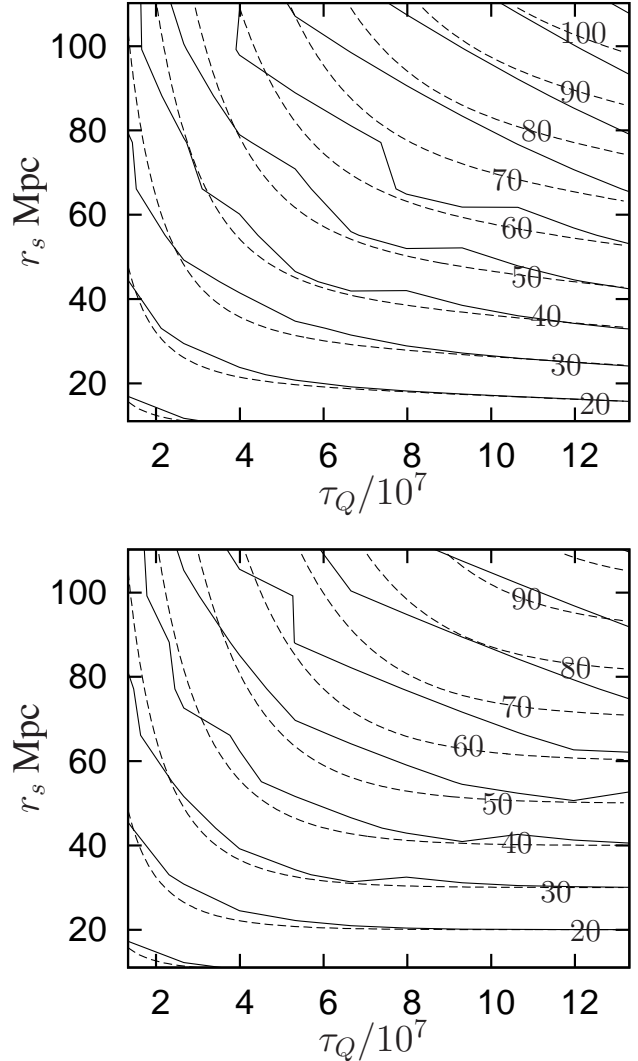


Figure 6. Contours of R_{\perp} (dashed lines) and R_f (solid lines) in comoving Mpc, shown for Models (i) and (ii) in the bottom and top panels respectively. R_f (defined in Section 4) is the radius of the spherical bubble that best matches an anisotropic bubble with parameters r_s and τ_Q .

R_{\perp} . Further, we use

$$\eta = \frac{R_{\parallel}}{R_{\perp}} - 1 \quad (9)$$

to quantify the anisotropy of the bubble. A value $\eta > 0$ indicates that the bubble appears elongated along the LOS, whereas $\eta < 0$ indicates that it appears compressed along the LOS. We have calculated R_{\perp} , s and η for a range of r_s and τ_Q , for which the results are shown in the contour plots of Figures 6, 7 and 8 respectively. The r_s , τ_Q range was chosen so that the largest bubble has a comoving radius roughly in the range 70 – 80 Mpc.

In our models the bubble, as viewed in the quasar's rest-frame, has a short period of rapid growth $\tau < 10^7$ yr beyond which it saturates (Model (i)) or grows slowly (Model (ii)) (Figure 2). Naively one would expect the bubble's image in redshifted 21-cm maps to exhibit a similar behavior. However, we see that the bubble's image continues to grow (Figure 6) well beyond $\tau = 10^7$ yr. The effect is more for larger bubbles where the light travel time is longer. The shift and anisotropy also are non-zero well beyond the period of the bubble's actual growth. For a fixed r_s , the shift decreases monoton-

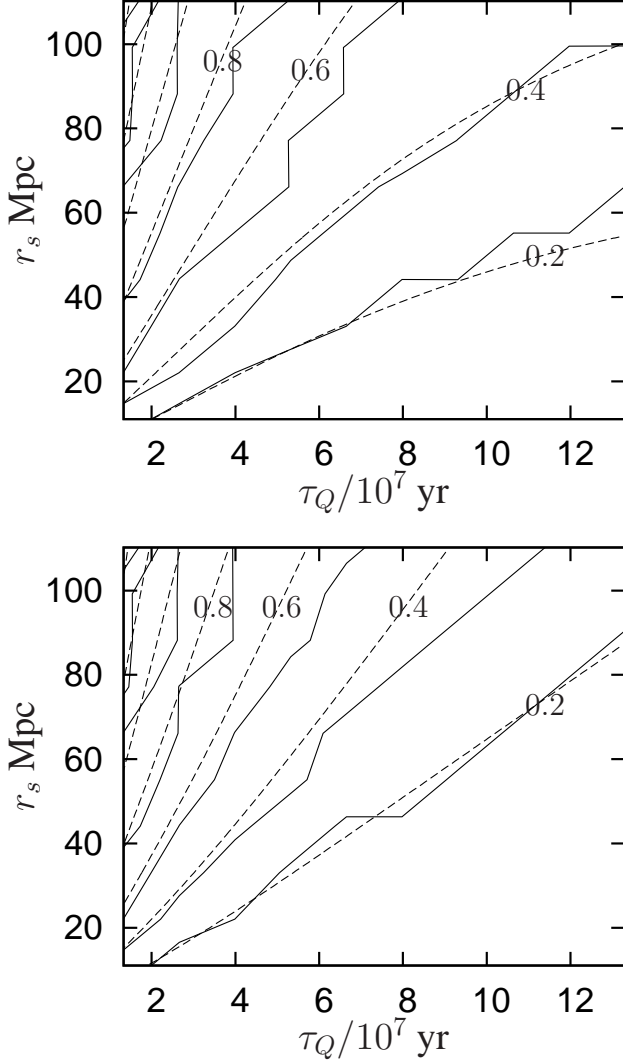


Figure 7. The dashed lines show contours of the shift parameter s defined by Eq. (8). The solid lines show contours of s_o which quantifies the shift between the center of the best matched filter and the quasar (defined in Section 4.). Models (i) and (ii) are shown in the bottom and top panels respectively.

ically with increasing τ_Q . While the shift can be as large as $s \geq 1$ (Figure 7) for a large bubble seen in an early phase of its growth, the typically value of s is in the range $0.2 \leq s \leq 0.6$. The bubbles appear elongated ($\eta > 0$), in the early phase of their growth (Figure 8). For a fixed τ_Q , we have more anisotropy for a larger bubble. The elongation diminishes with increasing τ_Q . This is followed by a situation where the bubble appears compressed ($\eta < 0$) along the LOS. This occurs when a bubble is viewed in the late stage of its growth where most of the bubble, except a small part of the back surface, has nearly stopped growing. The transition from an elongated bubble to a compressed bubbles is clearly visible in Figure 4. For both Models (i) and (ii), by and large, we expect the bubbles to be compressed with anisotropies of the order of $|\eta| \approx 0.1$ in Model (i), and somewhat larger anisotropies in Model (ii). Elongated bubbles may have anisotropies of the order $\eta \approx 0.1 - 0.5$, but these will be seen only in bubbles surrounding recently triggered quasars.

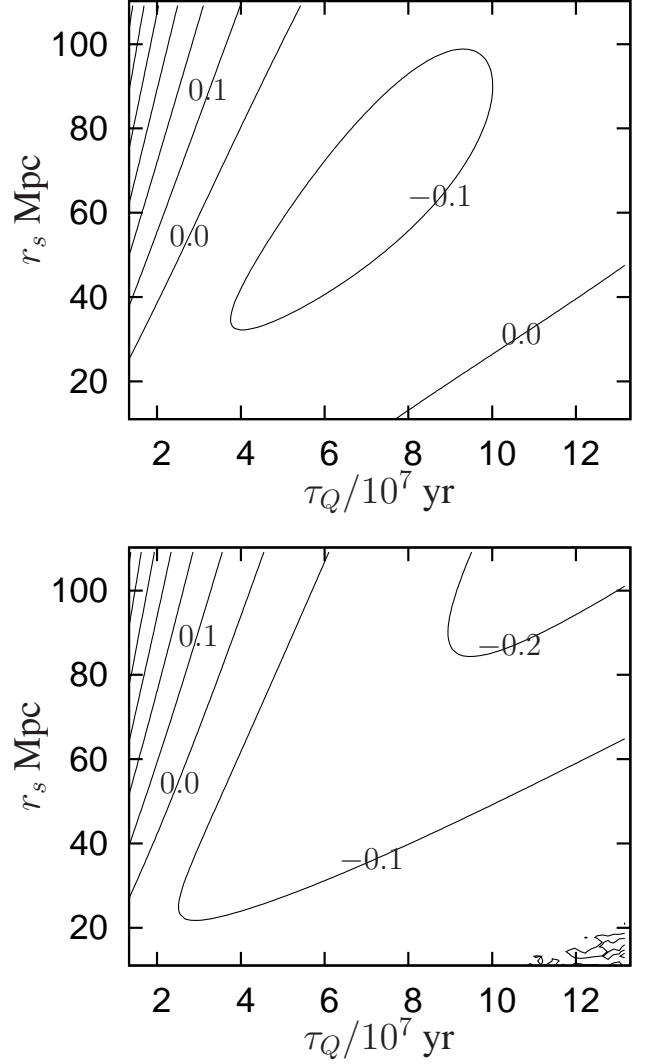


Figure 8. This shows contours of the anisotropy parameter η (defined by Eq. (9)) for Models (i) and (ii) in the bottom and top panels respectively. The contours are at an interval of 0.1.

3 MATCHED FILTER BUBBLE DETECTION TECHNIQUE

The quantity measured in radio-interferometric observations is the visibility $V(\vec{U}, \nu)$ which is related to the specific intensity pattern on the sky $I_\nu(\vec{\theta})$ as

$$V(\vec{U}, \nu) = \int d^2\phi A(\vec{\theta}) I_\nu(\vec{\theta}) e^{2\pi i \vec{\theta} \cdot \vec{U}} \quad (10)$$

Here the baseline $\vec{U} = \vec{d}/\lambda$ denotes the antenna separation \vec{d} projected in the plane perpendicular to the line of sight in units of the observing wavelength λ , $\vec{\theta}$ is a two dimensional vector in the plane of the sky with origin at the center of the FoV (*i.e.* phase center), and $A(\vec{\theta})$ is the beam pattern of the individual antenna. For the GMRT this can be well approximated by Gaussian $A(\vec{\theta}) = e^{-\theta^2/\theta_0^2}$ where $\theta_0 \approx 0.6 \theta_{\text{FWHM}}$.

The visibility recorded in a radio-interferometric observations is actually a combination of several contributions

$$V(\vec{U}, \nu) = S(\vec{U}, \nu) + HF(\vec{U}, \nu) + N(\vec{U}, \nu) + F(\vec{U}, \nu). \quad (11)$$

where the first term $S(\vec{U}, \nu)$ is the expected signal of the ionized

region that we are trying to detect. Note that the signal from an ionized region appears as a decrement with respect to the uniform background 21-cm radiation. This uniform background is however recorded only by the baseline at zero spacing which is usually not considered in radio-interferometric observations. Readers are referred to Paper I (section 2) for more detail regarding how to calculate $S(\vec{U}, \nu)$. $HF(\vec{U}, \nu)$ is the contribution from fluctuations in the H I distribution outside the ionized bubble, $N(\vec{U}, \nu)$ and $F(\vec{U}, \nu)$ are the noise and foreground contributions respectively.

The signal from an ionized bubble is expected to be buried deep under the other contributions (noise and foreground) which typically are orders of magnitude larger. We introduce an estimator $\hat{E}[\theta_x, \theta_y, z_b, R_b]$ to search if a particular ionized bubble (with bubble parameters $[\theta_x, \theta_y, z_b, R_b]$) is present in our observation. The estimator combines all the visibilities weighted by a filter $S_f(\vec{U}, \nu)[\theta_x, \theta_y, z_b, R_b]$,

$$\hat{E} = \sum_{a,b} S_f^*(\vec{U}_a, \nu_b) \hat{V}(\vec{U}_a, \nu_b). \quad (12)$$

Note that in order to keep the notation compact we do not explicitly show the parameters $[\theta_x, \theta_y, z_b, R_b]$ and $\hat{V}(\vec{U}_a, \nu_b)$ represents the observed visibility. The filter is designed (Paper I) to optimally combine the signal corresponding to the bubble that we are trying to detect while minimizing the contribution from the other contaminants. The expectation value of \hat{E} is

$$\langle \hat{E} \rangle = \sum_{a,b} S_f^*(\vec{U}_a, \nu_b) S(\vec{U}_a, \nu_b). \quad (13)$$

The other contributions to \hat{V} are assumed to be random variables of zero mean, uncorrelated to the filter, and hence they contribute only to the variance

$$\langle (\Delta \hat{E})^2 \rangle = \langle (\Delta \hat{E})^2 \rangle_{HF} + \langle (\Delta \hat{E})^2 \rangle_N + \langle (\Delta \hat{E})^2 \rangle_F \quad (14)$$

where the subscripts HF, N, F respectively refer to the contributions from the H I fluctuations, noise and foregrounds. The signal to noise ratio for the estimator is defined as

$$\text{SNR} = \frac{\langle \hat{E} \rangle}{\sqrt{\langle (\Delta \hat{E})^2 \rangle}} \quad (15)$$

Bubble detection will be carried out by analyzing the SNR for filters with different values of the parameters $[\theta_x, \theta_y, z_b, R_b]$. If an ionized bubble is actually present in the FoV, the SNR will peak when the filter parameters exactly match the parameters of the bubble. We shall have a statistically significant bubble detection if the peak $\text{SNR} \geq 3$ or $\text{SNR} \geq 5$ for a 3σ or 5σ detection respectively.

While the filter assumes the bubble to be spherical, it is evident from the previous section that bubbles are expected to appear anisotropic in redshifted 21-cm maps. It is in principle possible to introduce the anisotropy as an additional search parameter. This, however, would be required for preliminary bubble detection only if there is a severe mismatch between the spherical filter and the anisotropic image resulting in considerable degradation of the SNR.

4 RESULTS

In order to keep the computational time of the present investigation within bounds we consider a targeted search along the LOS to a known high z quasar. The FLTT does not affect the angular position of the bubble's center. and θ_x, θ_y will coincide with the

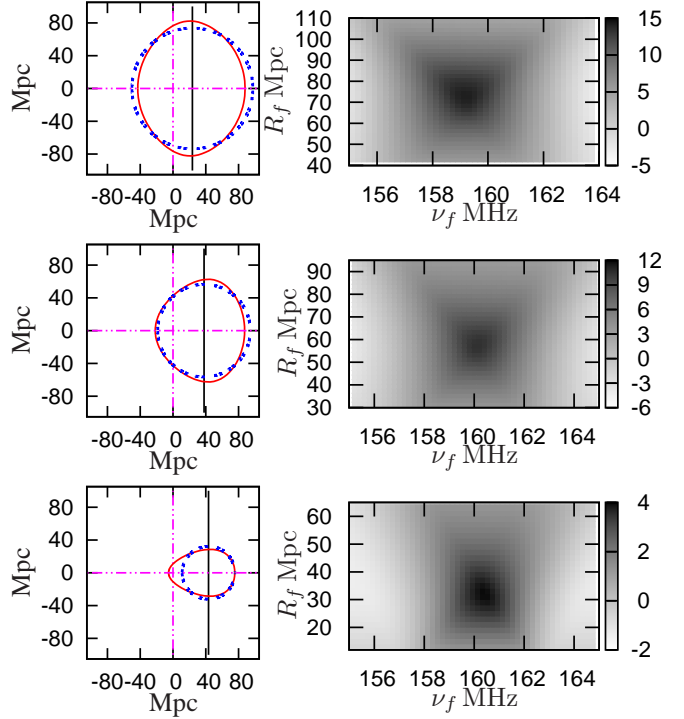


Figure 9. This shows anisotropic shapes and corresponding expected SNR contours for Model (i) considering 1000 hrs of observation with GMRT. From bottom to top solid curves in the left panels correspond to different apparent shapes of ionized regions for $\tau_Q = (1.3, 5.3, 10.6) \times 10^7$ yr respectively with $r_s = 88$ Mpc. The dotted curves represent spherical filters for which the SNR is maximum for the shape in that corresponding panel. Intersecting point of the dash-dotted lines represent position of the quasar and intersecting point of the dash-dotted and solid lines represent position of the filter center. Right panels show the matched filter SNR contours for corresponding left panel anisotropic shapes as function of filter radius R_f and filter center frequency coordinate ν_f .

angular position of the quasar. We consider a search varying the parameters R_f and ν_f which respectively correspond to the filter radius and the position of the filter's center along the LOS. In the bottom panels of Figure 9 we have explicitly shown the result for a situation where a bubble with parameters $r_s = 88$ Mpc and $\tau_Q = 1.3 \times 10^7$ yr is present surrounding a quasar which is located at $\nu_Q = 158$ MHz in the center of the FoV. The right panel shows the SNR for a search in the parameters ν_f and R_f . We find that the SNR peaks at $\nu_f = 160.4$ MHz and $R_f = 32$ Mpc, with $\text{SNR} = 3.99$ for 1000 hr of observation. The shape of the best match filter is shown in the left panel along with the bubble's apparent shape. The middle and top panels consider the same bubble at two later stages of its growth. We see that the bubble, which appears elongated ($\eta = 0.48$) in the bottom panel, becomes compressed in the middle and top panels ($\eta = -0.11, -0.2$ respectively). In all cases the best matched filter provides a reasonably good representation of the bubble that is actually present. The mismatch between the filter and the bubble that is actually present causes the SNR to be lower than that which is expected if the image of the bubble were spherical.

We have considered bubble detection for a range of r_s and τ_Q values for which the radius of the best match filter R_f are shown in Figure 6. Figure 7 shows the observed shift $s_o = (r_Q - r_c)/R_f$ where r_Q and r_c are the comoving distances to the quasar and the

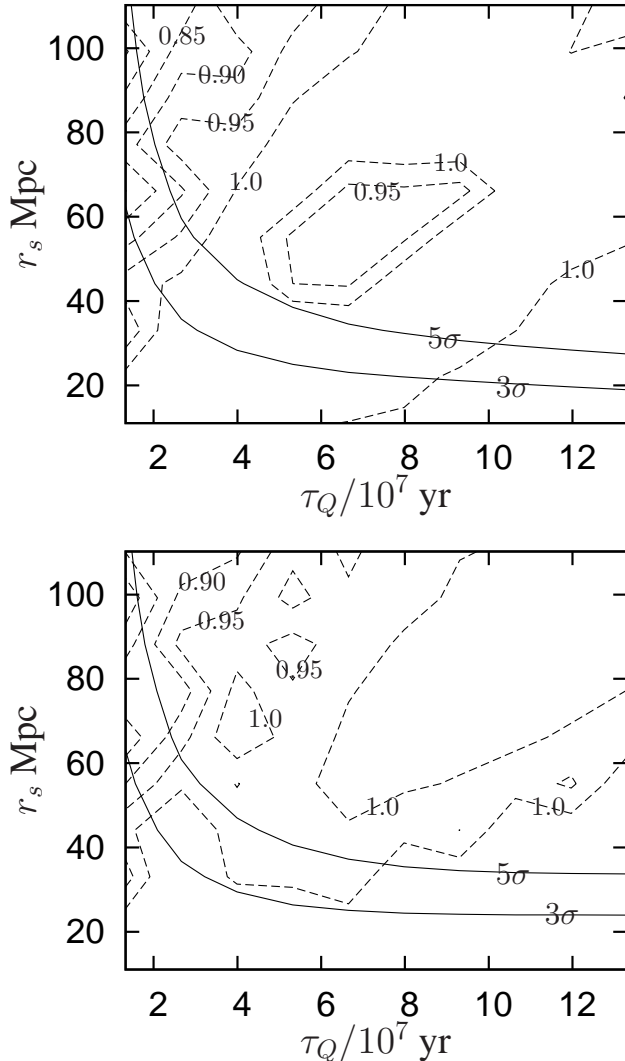


Figure 10. The dashed contours show f (defined in Section 4.), while the solid contours demarcate the regions where a 3σ and 5σ detection is possible. The bottom and top panels show results for Models (i) and (ii) respectively.

center of the filter respectively. We see that for most of the parameter space R_f and s_o for the best match filter closely follow R_{\perp} and s of the corresponding bubble image.

The situation where both the bubble and the corresponding quasar have been detected presents an interesting possibility. Both R_f and s_o are known in such a situation. The curves corresponding to constant R_f and s_o are non-degenerate, and it is possible to locate a unique point in the $r_s - \tau_Q$ parameter space once R_f and s_o are known. This holds the possibility of allowing us to estimate the age of the quasar responsible for the bubble. While the age estimate would depend on the model assumed for the photon emission rate, our analysis considering two different models indicates that we do not expect this variation to be very large.

The mismatch between the anisotropic bubble and the spherical filter is expected to cause a reduction in the SNR. For the best match filter Figure 10 shows the ratio f of the SNR for an anisotropic bubble to the SNR for a spherical bubble with the same R_f . We find that this ratio has value in the range $f \approx 0.9 - 1.0$ for nearly the entire parameter space that we have considered. There

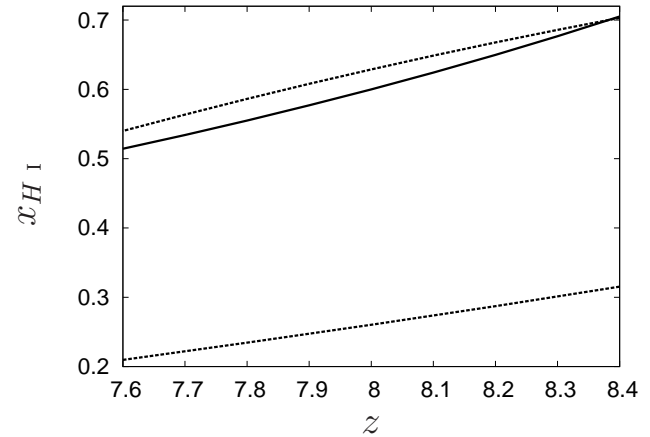


Figure 11. This shows the evolution of $x_{H I}$ across the redshift range that is relevant for the growth and detection of a bubble with $z_Q = 8$. The lower and upper dotted curves respectively show the early and late reionization models proposed by Choudhury & Ferrara (2005, 2006). The solid curve shows the model adopted for our analysis.

is a small region with small τ_Q , which corresponds to rapid bubble growth, where the ratio is in the range $f \approx 0.8 - 0.9$. We note that this matches with the region where the anisotropy is large $\eta \geq 0.4$. For 1000 hr of observations with the GMRT, the r_s , τ_Q range for 3σ and 5σ detection are shown in Figure 10. The smallest filter radius (comoving) for a 3σ and 5σ detection are approximately 24 Mpc and 33 Mpc respectively, which matches with the corresponding values when the finite light travel time is not taken into account.

4.1 Anisotropy due to evolving $x_{H I}$

The entire analysis, till now, assumes a fixed neutral fraction $x_{H I} = 0.6$ outside the bubble. The apparent anisotropy of a spherical bubble will, in principle, be affected by the evolution of $x_{H I}$. The bubble's front surface which is seen at a lower redshift will have a lower neutral fraction compared to the back surface. This will further increase the difference between the radius of the front and back surfaces as compared to the situation where $x_{H I} = 0.6$ for which the results have been shown in Figure 3 and 4.

The evolution of $x_{H I}$ during reionization is largely unknown, and there exists a wide range of evolution histories all of which are consistent with the presently available observational constraints. The lower and upper dotted curves in Figure 11 respectively shows the early and late reionization models proposed by Choudhury & Ferrara (2005, 2006). The entire region bounded by these two curves is consistent with the current observational constraints. To assess the impact of $x_{H I}$ evolution on bubble detection we have considered a simple model (the solid curve in Figure 11) where $x_{H I}^{-1}$ evolves linearly in the vicinity of $z = 8$. We do not expect $x_{H I}$ to decline very rapidly around $z = 8$, and the slope has been chosen so as to approximately match those of the two dotted curves in Figure 11.

The subsequent discussion of this subsection is entirely restricted to the largest bubble ($r_s = 100$ Mpc) for which the bubble's comoving radius grows to 100 Mpc by $\tau = 10^8$ yr when $x_{H I}$ is constant at 0.6. The bubble's apparent image spans from $z = 8.2$ to 7.6, and $x_{H I}$ changes from 0.64 to 0.52 across the bubble in the evolving $x_{H I}$ model that we have considered. For

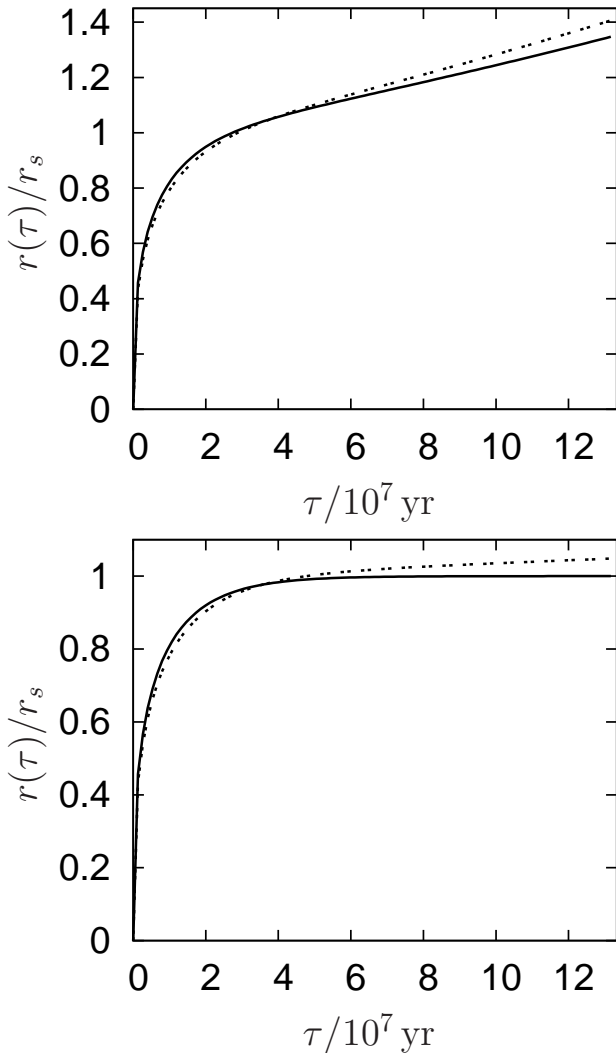


Figure 12. This dotted curve shows the growth of an H II bubble for our model of evolving global neutral fraction. The quasar age is set to $\tau_Q = 1.3 \times 10^8$ yr at $z = 8$. The results for a constant neutral fraction $x_{H\text{I}} = 0.6$ are shown for comparison (solid curve). The bottom and top panels respectively correspond to Models (i) and (ii).

the same model, $x_{H\text{I}}$ is 0.7 at the redshift where the bubble is born if the quasar has an age of $\tau_Q = 1.3 \times 10^8$ yr at $z = 8$.

We have modified eq. (1) to incorporate the evolution of $x_{H\text{I}}$ (see Appendix A for details) for which Figure 12 shows the growth of the bubble’s comoving radius. For both Models (i) and (ii) we find that incorporating the evolution of $x_{H\text{I}}$ initially slows the growth of the bubble relative to the situation where $x_{H\text{I}}$ is constant. This is reversed in the later stages where the growth is enhanced with respect to the situation where $x_{H\text{I}}$ is constant. For the parameter range that we have considered, the difference in the bubble radius due to the evolution of $x_{H\text{I}}$ is found to be less than 5%. Further, there is a significant difference only at the later stages of the bubble’s growth ($\tau > 3\tau_{rec} \sim 4 \times 10^7$ yr). We next consider the effect of the evolution of $x_{H\text{I}}$ on the anisotropy and shift parameters η and s (Figure 13). We find that the effect is maximum when the bubble is seen in the late stage of its growth where the apparent image is compressed along the line of sight. The evolution of $x_{H\text{I}}$ acts to reduce the compression and increase the shift rela-

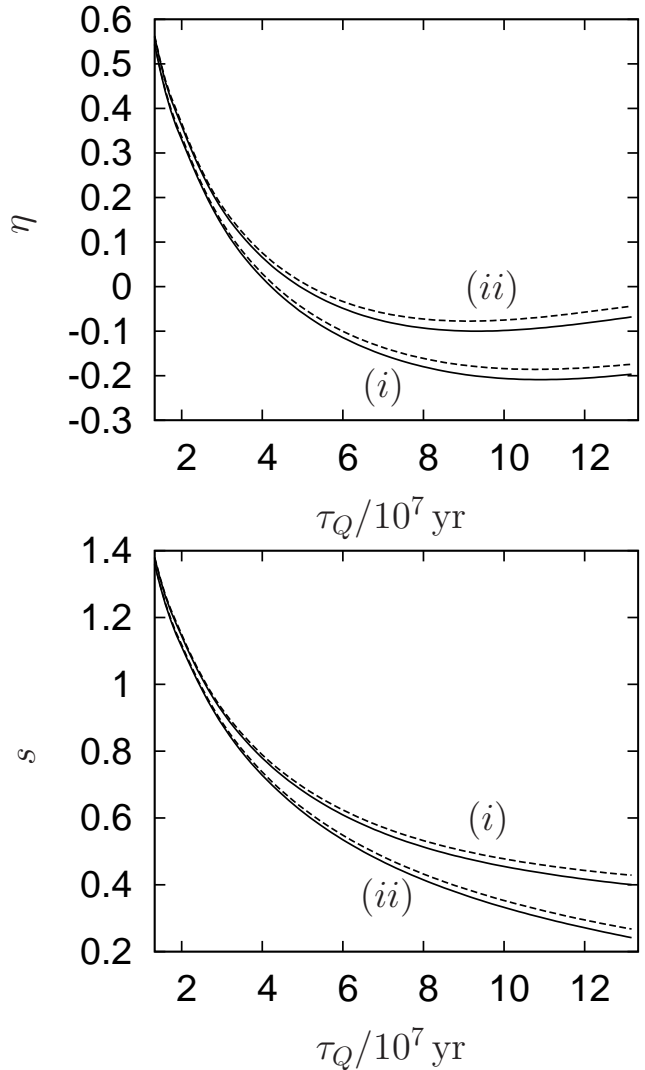


Figure 13. This shows the variation of η (top panel) and s (bottom panel) with τ_Q for an H II bubble with $r_s = 100$ Mpc. In both panels the solid and dashed curves represent the constant and evolving $x_{H\text{I}}$ models respectively. The two different sets of curves in each panel correspond to Models (i) and (ii) respectively.

tive to a situation where $x_{H\text{I}}$ is constant. The maximum change is found to be around 10%. This change in the anisotropy has a very small impact on matched filter bubble detection. The radius of the best matched filter, we find, changes by less than 5% whereas the corresponding SNR changes by less than 1%. The changes being extremely small, we have not explicitly shown these results.

The discussion till now has focused on a large bubble with $r_s = 100$ Mpc. The effect of the evolution of $x_{H\text{I}}$ will be less for smaller bubbles.

5 SUMMARY & CONCLUSIONS

The apparent image of a quasar generated, spherical ionized region appears anisotropic due to the finite light travel time and the evolution of the global neutral fraction. We have quantified this anisotropy and assessed its impact on matched filter bubble detection in redshifted 21-cm maps at $z = 8$. We find that the anisotropy is less than 20% for most of the parameter space that we have con-

sidered. Further, the bubble appears compressed along the LOS for nearly the entire parameter range where a detection is possible. In addition to the anisotropy, the bubble's center is also shifted from the actual position of the quasar along the LOS. This shift, which can be rather large and may exceed the bubble radius, typically varies across the range 20 – 80%. We find that these effects do not cause a significant degradation of the SNR in matched filter bubble search and spherical filters are adequate for a preliminary bubble detection. We show that such a detection where the radius of the best match filter, its center and the quasar redshift are all known can be used to estimate τ_Q the age of the quasar. This detection also provides an estimate of the neutral fraction $x_{H\text{ I}}$ provided the quasar luminosity is known. Follow up observations, subsequent to a detection, can in principle be used to measure the anisotropy which would impose further constraints on the quasar luminosity, τ_Q and $x_{H\text{ I}}$. The global neutral fraction is not expected to evolve very rapidly with z around $z = 8$, and this makes a rather small change ($< 10\%$) for the anisotropy and the shift relative to a situation where $x_{H\text{ I}}$ is constant.

An earlier work (Paper III) has shown that both the GMRT or the MWA are most sensitive to the signal from an ionized bubble if it is at a redshift $z \sim 8$. At this z a bubble of comoving radius ≥ 24 Mpc and ≥ 33 Mpc can respectively be detected at 3σ and 5σ significance with 1000 hrs of observation. This, however, presupposes the presence of an ionized bubble located near the center of the FoV. It is, however, necessary to take into account the abundance of ionized bubbles when considering possible observational strategies.

How many H II bubbles do we expect to find above the detection threshold in a single GMRT observational volume at redshift $z = 8$? There is, till date, no quasar detected with $z > 6.4$, though there are galaxies which have been detected at $z > 8$ (eg. Lehnert et al. (2010)) and it is quite likely that quasars may be detected in the near future. At present one thus typically uses theoretical models which correctly predict the observed quasar abundance and evolution at $z \leq 6$ to predict the expected number of detectable quasar H II bubbles at higher redshifts, though these predictions are highly model dependent and uncertain (Rhook & Haehnelt, 2006). Predictions based on the CDM merger driven model (Wyithe & Loeb, 2003; Wyithe, Loeb & Barnes, 2005; Rhook & Haehnelt, 2006) indicate that we expect ~ 1 ionized bubble of comoving radius ≥ 20 Mpc around an active quasar in 400 degree² and 16 MHz volume. This means that the probability of a detection is less than 5% in a single random GMRT observation volume (~ 10 degree² and 32 MHz) at redshift $z = 8$. Including the possibility of fossil bubbles whose quasars have switched off increases the number of H II bubbles (Wyithe, Loeb & Barnes, 2005), and we expect ~ 5 detectable bubbles in a random GMRT observation. Note that, the shape of these fossil bubbles would not be distorted due to the FLTT as they have ceased to grow.

The typical size of quasar generated H II bubbles at $z \sim 8$ is an important factor in matched filter bubble detection. Maselli et al. (2007) predict the comoving radius of quasar generated H II regions to be ~ 45 Mpc at $z = 6.1$ with $x_{H\text{ I}} = 0.1$. This size is expected to be less at $z \sim 8$ where the global neutral fraction is higher. The typical radius of a galaxy generated bubble is expected to be ~ 10 comoving Mpc at $z \sim 8$ (McQuinn et al., 2007). These galaxy generated bubbles outside the quasar generated bubble that is targeted for detection will contribute to the fluctuations in the matched filter estimator \hat{E} . However, simulations (Paper II) indicate that small bubbles of size 10 Mpc will not have much impact on detection in the range (≥ 24 Mpc) where a detection is feasible.

Finally, we note that there are various other sources of anisotropy such as the spatial fluctuations in the neutral hydrogen distribution due to galaxy generated ionized bubbles, anisotropic emission from the quasar itself which have been ignored. Galaxy generated ionized bubbles in the surrounding IGM can cause significant anisotropies in the quasar generated ionized bubbles. One needs to use detailed simulation to investigate this which is beyond the scope of this paper. We plan to address these issues in future.

6 ACKNOWLEDGMENTS

We would like to thank the anonymous referee for providing us with constructive comments and suggestions which helped to improve the paper. SM would like to thank Prasun Dutta, Prakash Sarkar, Tapomoy Guha Sarkar, Subhasis Panda, Abhik Ghosh and Sanjit Das for useful discussions. KKD is grateful for financial support from Swedish Research Council (VR) through the Oscar Klein Centre.

References

- Bharadwaj, S., & Pandey, S. K. 2005, MNRAS, 358, 968
 Choudhury, T. R., & Ferrara, A., 2005, MNRAS, 361, 577
 Choudhury, T. R., Ferrara, A., 2006, Cosmic Polarization, Editor - R. Fabbri (Research Signpost), p. 205, arXiv:astro-ph/0603149
 Choudhury, T. R., 2009, Current Science, 97, 6, 841
 Datta, K. K., Bharadwaj, S., & Choudhury, T. R., 2007, MNRAS, 382, 109
 Datta, K. K., Majumdar, S., Bharadwaj, S., & Choudhury, T. R., 2008, MNRAS, 391, 1900
 Datta, K. K., Bharadwaj, S., & Choudhury, T. R. 2009, MNRAS, 399, L132
 Furlanetto, S. R., Zaldarriaga, M. & Hernquist, L. 2004, ApJ, 613, 1
 Furlanetto, S. R., Oh, S. P. & Briggs, F. H., Phys. Rep. 2006, 433, 181
 Geil, P. M., & Wyithe, J. S. B. 2008, MNRAS, 386, 1683
 Geil, P. M., Wyithe, J. S. B., Petrovic, N., & Oh, S. P. 2008, MNRAS, 390, 1496
 Lehnert, M. D., et al. 2010, Nature, 467, 940
 Maselli, A., Gallerani, S., Ferrara, A., & Choudhury, T. R. 2007, MNRAS, 376, L34
 McQuinn, M., Lidz, A., Zahn, O., Dutta, S., Hernquist, L., & Zaldarriaga, M. 2007, MNRAS, 377, 1043
 Rhook, K. J., & Haehnelt, M. G. 2006, MNRAS, 373, 623
 Sethi, S., & Haiman, Z. 2008, AJ, 673, 1S
 Shapiro, P. R., & Giroux, M. L. 1987, ApJL, 321L, 107S
 Shapiro, P. R., Iliiev, I. T., Alvarez, M. A., & Scannapieco, E. 2006, ApJ, 648, 922
 Swarup G., Ananthkrishnan S., Kapahi V.K., Rao A.P., Subramanya C.R., Kulkarni V.K., 1991 Curr.Sci., 60, 95
 White, R. L., Becker, R. H., Fan, X., & Strauss, M. A. 2003, AJ, 126, 1
 Wyithe, J. S. B., & Loeb, A., 2003, ApJ, 595, 614
 Wyithe, J. S. B., & Loeb, A. 2004, ApJ, 610, 117
 Wyithe, J. S. B., Loeb, A., & Barnes, D. G. 2005, ApJ, 634, 715
 Yu, Q., & Tremaine, S. 2002, MNRAS, 335, 965
 Yu, Q., & Lu, Y. 2004, ApJ, 610, 93
 Yu, Q. & Lu, Y. 2005, ApJ, 620, 31

Yu, Q. 2005, ApJ, 623, 683

APPENDIX A: GROWTH EQUATION FOR H II BUBBLE CONSIDERING EVOLVING NEUTRAL FRACTION

Here we consider the growth of an H II bubble embedded in a medium whose neutral fraction $x_{H\text{ I}}$ outside the bubble is evolving. The evolution of the neutral fraction is parameterized using

$$x_{H\text{ I}}(\tau) = x_{H\text{ I}}(\tau_Q) f(\tau) \quad (\text{A1})$$

where $x_{H\text{ I}}(\tau_Q)$ is the neutral fraction at the redshift $z_Q = 8$, and the function $f(\tau)$ which quantifies the evolution satisfies $f(\tau_Q) = 1$. Further, the ionizing photon emission rate of the quasar is expressed as $\dot{N}_{phs} = \dot{N}_{phs,i} s(\tau)$ with $s(\tau) = 1$ for Model (i) and $s(\tau) = \exp(\tau/\tau_s)$ for Model (ii). Using these, the equation governing the growth of an ionized bubble (eq. 1) may be written as

$$\frac{d}{d\tau} (r^3 f) = \frac{r_s^3 s}{\tau_{rec}} - \frac{r^3}{\tau_{rec}} \quad (\text{A2})$$

where τ_{rec} and r_s are constants calculated using eq. (3) and eq. (6) respectively using $x_{H\text{ I}}(\tau_Q)$ i.e. value of $x_{H\text{ I}}$ at $z = 8$. Note that we have ignored the effect of the finite light travel time from the quasar to the ionization front on $f(\tau)$. We then have the solution

$$r(\tau) = r_s \left\{ \frac{1}{f(\tau)} \int_0^\tau \frac{d\tau'}{\tau_{rec}} \exp \left[-\frac{1}{\tau_{rec}} \int_0^{\tau-\tau'} \frac{d\tau''}{f(\tau'')} \right] s(\tau') \right\}^{\frac{1}{3}}. \quad (\text{A3})$$

The analysis is considerably simplified if we approximate the evolution of the neutral fraction as

$$\frac{1}{f(\tau)} = 1 + b \left(\frac{\tau - \tau_Q}{\tau_{rec}} \right) \quad (\text{A4})$$

whereby eq. (A3) can be written in terms of a single integral as

$$r(\tau) = r_s \left\{ \left[1 + b \left(\frac{\tau - \tau_Q}{\tau_{rec}} \right) \right] \int_0^\tau \exp \left[-\left(\frac{\tau - \tau'}{\tau_{rec}} \right) \left(1 - b \frac{\tau_Q}{\tau_{rec}} - \frac{b}{2} \left(\frac{\tau - \tau'}{\tau_{rec}} \right)^2 \right) \right] s(\tau) \frac{d\tau'}{\tau_{rec}} \right\}^{\frac{1}{3}} \quad (\text{A5})$$

The integral in eq. (A5) can be easily evaluated numerically. We use this equation to study the growth of an H II bubble for a wide range of values of the parameters r_s and τ_Q , taking into account the variation of the neutral fraction. It is quite evident that we recover eqs. (4) and (5) in the situation where $b = 0$ i.e. the neutral fraction does not evolve.

The evolution of the neutral fraction $x_{H\text{ I}}$ is largely unknown at the redshifts $z \sim 8$. For the purpose of our discussion we consider two models proposed by Choudhury & Ferrara (2005, 2006) which implements most of the relevant physics governing the thermal and ionization history of the IGM through a semi-analytical formalism. Figure 11 shows the predicted evolution of $x_{H\text{ I}}$ over the relevant z range. For the subsequent analysis in this paper we have used $b = 0.015$ in eq. (A4) whereby the predicted $x_{H\text{ I}}(z)$ is in rough consistency with the evolution allowed by the two models.

The growth of an H II bubble with evolving $x_{H\text{ I}}$ (dotted line) has been shown in Figure 12 for both Model (i) and (ii) of photon emission rate. For comparison with our previous analysis in this paper, growth for constant $x_{H\text{ I}}$ (solid line) is also shown in the same figure.